Optical Materials 128 (2022) 112456

Contents lists available at ScienceDirect

Optical Materials

journal homepage: www.elsevier.com/locate/optmat

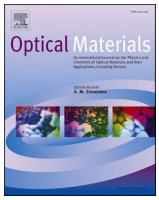

Impact of Au nanoparticles on the thermophysicalparameters of Fe_3O_4 nanoparticles for seawater desalination

M. Nabil [a,*], Horia F [a], S.S. Fouad [b], Sohair Negm [a]

[a] Department of Basic Engineering Sciences, Faculty of Engineering (Shoubra), Benha University, Cairo, Egypt
[b] Department of Physics, Faculty of Education, Ain Shams University, Cairo, 11566, Egypt

ARTICLE INFO

Keywords:
Nanocomposite
Photoacoustic spectroscopy
Thermal desalination
Thermal efficiency

ABSTRACT

The objective of the present study is to investigate the impact of gold nanoparticles (Au NPs) on the thermo-optical parameters of Fe_3O_4 (NPs), which can be used in seawater desalination cycles. The SEM and the EDX were used to obtain the compositional structure. The observed optical characteristic peaks of UV–visible absorption spectra depend mainly on the size of the particle and the suspension medium. With the addition of AuNPs, both the optical direct band gap (E_g) and the electronegativity decreased, while the refractive index increased. The deep analysis of the optical conductivities has revealed the influence of seawater conductivity on the efficiency. The morphology and structural investigation and crystal size were performed by means of the (TEM), and (XRD), that showed a spherical shape structure for the Au/Fe_3O_4 NCs, corresponding to surface Plasmon of the Au NPs, and the exciting of Fe_3O_4 (NPs). A highly sensitive photoacoustic (PA) technique has been utilized to investigate the thermal parameters. Moreover, the (PA) technique, and the surface modification of Nano black particles using nonionic surfactant, were boosted with heat exchange and their values imply the possibility of improving the solar thermal conversion efficiency through the combination of morphological and elemental information of the addition of Au NPs to Fe_3O_4 (NPs).

1. Introduction

The shortage of the resources of freshwater, due to the increase of the population, made the desalination a global trend to unconventional water sources. The desalination is a feasible and reliable solution for having freshwater from seawater. Recently several attempts had been given by researchers to develop and reduce the coast desalination technology [1–4]. The (Fe_3O_4) magnetic nanoparticles (NPs) have been used successfully for brackish water desalination attracted, because of their broad range of photo thermal applications, extensive photon absorption cross-section, and strong intermolecular bonds [5–7]. Due to the movement of the sun, collectors require solar tracking, which is called direct absorption volumetric solar collectors [8–12]. Absorption of sunlight causes an increase in the molecule's vibration and hence increasing temperature. Most of the absorbed solar radiation is converted to solar energy [13–15]. It has been established that the metallic nanoparticles have unusual chemical and physical properties which make them suitable for desalination uses. Estimating freshwater nowadays is a major problem; therefore, desalination became a key factor for the sustainability of the world's population [16–19]. The purpose of the present article is to study the capability of adding Au NPs to Fe_3O_4 NPs on modifying optical properties, particle size and thermal parameters. Au NPs can produce particles of well-defined grain size. Additionally, the effect of the addition of surfactant on the efficiency of seawater is also investigated. The interrelation features between the optical parameters and the characterizations had been also discussed for improving the thermal efficiency of seawater desalination.

2. Experimental work

2.1. Synthesis of Fe_3O_4 NPs & Au/Fe_3O_4 NCs

Amalgamation of Fe_3O_4 magnetics nanoparticles (NPs) were set up by co-precipitation of ferric and ferrous salts under the nearness of N_2 gas. 16.25g $FeCl_3$ and 6.35 g of $FeCl_2$ were dissolving into 200 mL of refined water. Chemical precipitation was accomplished at 300 °C, after 60 min of vigorous stirring of mixing ammonium solution arrangement drop by drop. The completed precipitation of Fe_3O_4 at pH was achieved somewhere between 8 and 14 [20]. After the system was cooled to room temperature, the precipitates were isolated by a permanent magnet and

* Corresponding author.
E-mail address: mohammed_diab35@yahoo.com (M. Nabil).

https://doi.org/10.1016/j.optmat.2022.112456
Received 7 February 2022; Received in revised form 29 April 2022; Accepted 4 May 2022
Available online 14 May 2022

washed with deoxygenated refined water until pH neutral. Finally, nanoparticles of Fe_3O_4 NPs in powder form were prepared after being washed with acetone and dried in oven at 60–700 °C for 1 h. The Au/Fe_3O_4 Nanocomposite (NCs) particle was prepared by Co-precipitation method with hydroxylamine in the presence of Fe_3O_4 (NPs) as seeds. First, the seeds were made through the chemical co-precipitation of Fe (II) and Fe (III) ions in alkaline medium, followed by rinsing several times with water until the pH reached 6–7. An external magnetic field was used during the washing process. In order to absorb Au^{3+} onto Fe_3O_4 NPs, a 20.0 mL of 4.0 mg/mL Fe_3O_4 NPs was dispersed in 100.0 mL of 0.1 mol/L $HAuCl_2{\cdot}4H_2O$ solution in a beaker, and slowly mixed. Finally, 40.0 mL of NH_2OH solution of 80.0 mmol/L was added to the system, the mixture was continually shaken for 1 h to form the composite structure of Au/Fe_3O_4 NCs. Triton X-100 (TX100), which is a mixture of 4-t-octylphenoxyethoxyethanols with an average molecular weight of 625 Da (g/mole), was purchased from Sigma-Aldrich (MO, USA) and was used without purification. Its chemical formula is $(CH_3)_3CCH_2C(CH_3)_2C_6H_4O\text{-}(CH_2CH_2O)_pH$ with an average number p of ethylene oxide (EO) groups of 9.5. Its density is 1.065 g/cm^3.

The elemental composition of Fe_3O_4 NPs & Au/Fe_3O_4 NCs were investigated by the scanning electron microscope (SEM)(JOEL-JSM Model 5600) and Energy -dispersive X-ray spectroscopy (EDX) (Shim ADZU diffractometer type XRD 6000). The absorption spectra was obtained using (V-670 Jasco double-beam spectrophotometer). The particle size was identified by Transmission Electron microscope (TEM). The thermal parameters were investigated by using a highly sensitive (PA) (MTEC Model 300) [21–23]. Fig. 1(a) and (b) presents the schematic diagrams for the PA experimental set-up and the Au/Fe_3O_4 NCs in water desalination respectively.

The solution temperature was monitored by using an optical fiber probe model (FOBS) immersed in the solution and connected to digital meter model (OMEGA-FOB). A computer interface program is used for registering the temperature rise with time for the samples under study as shown in Fig. 1(c).

3. Results and discussion

3.1. SEM image and EDX analysis

The morphology and the crystalline structure are obtained by SEM & EDX. A high-resolution SEM micrograph of Au/Fe_3O_4 NCs is given in Fig. 2.

The inset of the SEM image illustrates the spherical nanoparticles. The observation of other small particles, indicate the successful synthesized of Au/Fe_3O_4 NCs. In addition, the components of the EDX spectra shows clearly the presence the peaks of Fe, O, and Au elements, and no other impurities were found in the samples. The weight percentage (wt.%) of Fe, O and Au for Au/Fe_3O_4 NCs are 71.25 wt%, 21.13 wt% and 7.62 wt% respectively.

3.2. UV- V absorption analysis

The UV–visible absorption spectra of Fe_3O_4 NPs and Au/Fe_3O_4 NCs are seen in Fig. 3 (a). The broad absorbance edge at ≈ 387 nm, may be due to the half-metallic behavior of Fe_3O_4 NPs [24,25]. Furthermore, Fe^{+3} of Fe_3O_4 could increase the light absorption from UV to visible

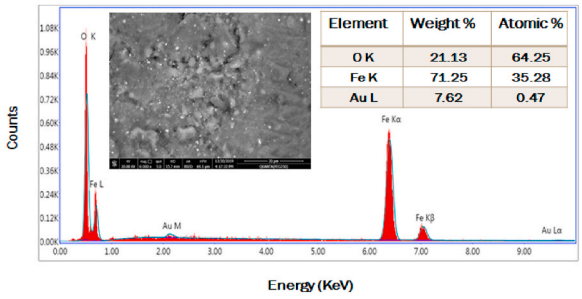

Fig. 2. EDX spectrum and the inset SEM image, weight percentage (wt.%) of Au/Fe_3O_4 NCs.

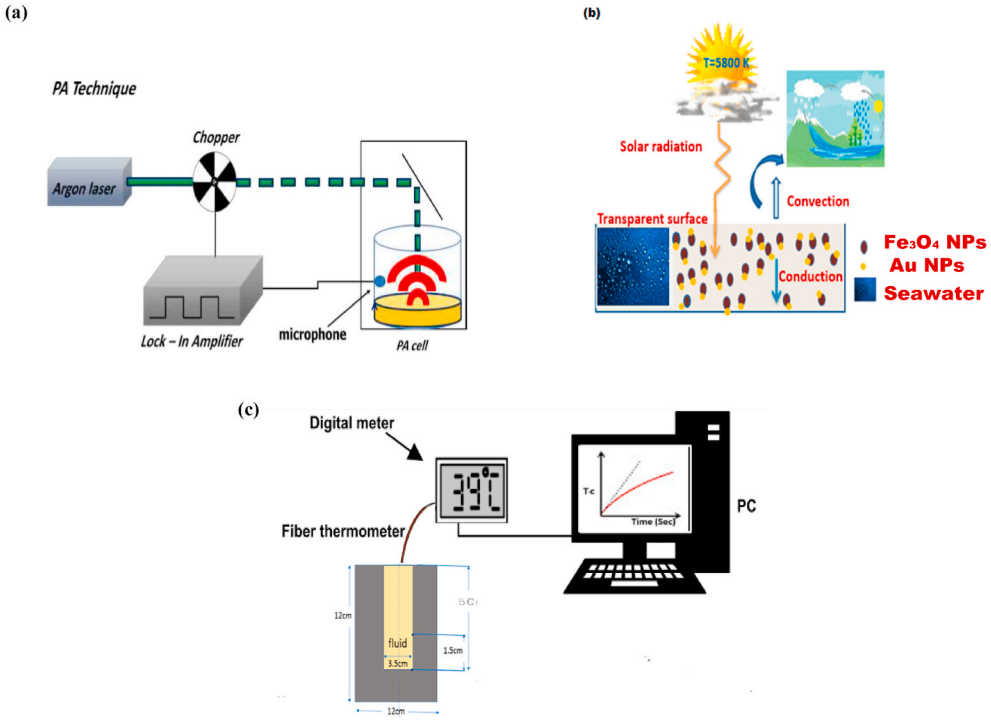

Fig. 1. (a) The PA experimental set-up diagram for thermal measurements, **(b)** Schematic showing how to use Au/Fe_3O_4 NCs in water desalination and **(c)** Experimental setup for registering the temperature rise with time.

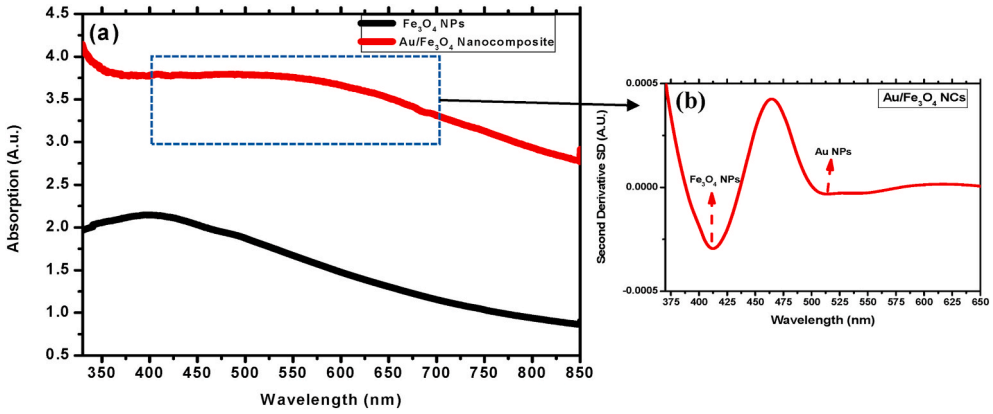

Fig. 3. (a) Absorption spectra of Fe_3O_4 NPs and Au/Fe_3O_4 NCs. **(b)**The second derivative (SD) of Au/Fe_3O_4 NCs.

region [26]. The observed peak around 524 nm, is corresponding to the Plasmon excitation in the Au (NPs). The results are in a good agreement with other materials contain surface plasmon properties [27–29]. The Au NPs act as an electron sink enhancing the charge separation in Fe_3O_4 NPs, that leads to increase the absorption of the Fe_3O_4 NPs in the visible region.

The second derivative analysis (SD) was used for determining the accurate peak position of Au/Fe_3O_4 NCs as seen in Fig. 3(b) for the two regions, Plasmon and the exciton. It is seen that the first absorption peak of Fe_3O_4 NPs red shifts from 387 nm to 413 nm, with the stability of the Plasmon absorption band of Au NPs (at 524 nm). The modification of electron oscillation of Au NPs as well as the increase of Fe_3O_4NPs absorption, were used for suppression the surface plasmon (SP) feature.

The optical absorption coefficient (**α**) is a crucial parameter in determining the electronic transition. The optical energy gap ($\mathbf{E_g}$) can be determined on basis of equation [30,31].

$$\boldsymbol{\alpha h\upsilon = A\left(h\upsilon - E_g\right)^r} \tag{1}$$

where ***(hυ)*** is the incident photon energy, ***(α)*** is the absorption coefficient, ***(A)*** is a constant, and (***r***) is an important factor that detects the type of existing transition where ***r*** may equal **2** or ½ for indirect or direct transition, respectively. The best fit obtained for $\boldsymbol{r = 1/2}$. Fig. 4 shows the alternation of $(\alpha h\nu)^2$ with the variation in photon energy **(hυ)** for the two samples Fe_3O_4 NPs and Au/Fe_3O_4 NCs. The direct (Eg) values of Fe_3O_4 NPs and Au/Fe_3O_4 NCs was estimated from the intercept of each line and are given in Table 1. In general, due to the relationship between the conductivity and the efficiency, when conductivity is 0 the efficient should be high, and hence on increasing the conductivity, the efficiency decreases. Conductivity is a measure of water's capability to pass electric flow. This ability is depending on many parameters among them the

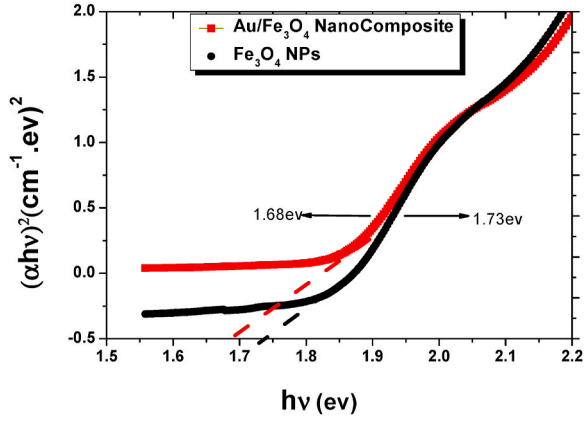

Fig. 4. $(\alpha h\nu^2)$ versus $(h\nu)$ for Fe_3O_4NPs and Au/Fe_3O_4 NCs samples.

absorption coefficient (**α**) and the refractive index (**n**). The refractive indices of Fe_3O_4 NP_S and Au/Fe_3O_4 NCs was calculated based on optical energy gap by using two different equation [32,33]:

$$\boldsymbol{n^4 E_g = 95eV} \tag{2}$$

And

$$\boldsymbol{n = 4.16 - 0.85E_g} \tag{3}$$

The data are summarized in Table 1. The average value of **n** determined from equations (2) and (3) as observed in Table 1, were found to increases with the addition of AuNPs. Interesting relationships have been found between the optical energy gap $\mathbf{E_g}$, optical electronegativity ($\boldsymbol{\chi_e}$) and **n**. The optical electronegativity is a key parameter for understanding the chemical bonding. As the electronegativity difference increases, so does the energy difference between bonding and antibonding. The electronegativity parameter ($\boldsymbol{\chi_e}$) can be estimated by substituting the obtained value of (**Eg**), into the empirical formula [34]:

$$\boldsymbol{\chi_e = 0.2688\, E_g} \tag{4}$$

Table 1, presents the value of the electronegativity as observed the variation of (**Eg**), (**n**) and ($\boldsymbol{\chi_e}$) reveals the correlation mentioned above. The optical conductivity ($\boldsymbol{\sigma_{opt}}$) can be determined by using the obtained value of the average refractive index and the velocity of light c from this equation [35]:

$$\boldsymbol{\sigma_{opt} = \frac{\alpha\, n\, c}{4\pi}} \tag{5}$$

The dependence of $\boldsymbol{\sigma_{opt}}$ on $\mathbf{h}\,\boldsymbol{\upsilon}$ is displayed in Fig. 5(a). As seen the $\boldsymbol{\sigma_{opt}}$ increases with increasing $\mathbf{h}\,\boldsymbol{\upsilon}$ and with the addition of Au NPs as well [36,37].

The sharp increase of the $\boldsymbol{\sigma_{opt}}$ after 3.50 eV, is in similar with the increase of the absorption coefficient. Pure water is not a good conductor of electricity, the electrical conductivity $\boldsymbol{\sigma_{elec}}$ of water is its ability to conduct an electric current. The $\boldsymbol{\sigma_{elec}}$ can be determined via the expression [38,39].

$$\boldsymbol{\sigma_{elec} = \frac{2\,\lambda\,\sigma_{opt}}{\alpha}} \tag{6}$$

A decrease in the electrical conductivity is noted with increasing photon energy as depicted in Fig. 5(b). In general, crystal size affects the mean free path and obviously affect the electrical conductivity.

3.3. Crystalline structure and surface morphology

TEM analysis was used for determining the average particle size of Fe_3O_4 NPs and Au/Fe_3O_4 NCs. The TEM micrographs of Fe_3O_4 NPs and Au/Fe_3O_4NCs are shown in Fig. 6(a) and (b) respectively. In Fig. 6 (a) A spherical morphology can be observed as gray color in the image of the

Table 1
The direct optical energy gap (E_g), Refractive index (n), optical electronegativity (χ_e) and the crystal size of Fe_3O_4 NPs and Au/Fe_3O_4 NCs.

Sample	Band gap E_g (eV)	*n*		Average (n)	χ_e	Crystal size (nm)		
		Eq (2)	Eq (3)			TEM	EMA	XRD
Fe_3O_4 NPs	**1.73**	**2.72**	**2.69**	**2.70**	**0.465**	**30**	**30.03**	**30.43**
Au/Fe_3O_4 NCs	**1.68**	**2.74**	**2.73**	**2.73**	**0.451**	**49**	**-**	**-**

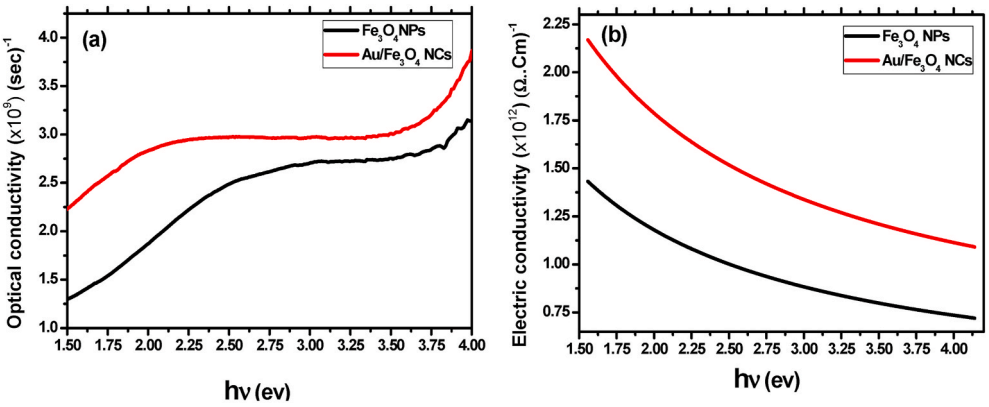

Fig. 5. **(a)** Optical conductivity versus (hν) plot for Fe_3O_4 NPs and Au/Fe_3O_4 NCs. **(b)** Electric conductivity versus (hν) plot for Fe_3O_4 NPs and Au/Fe_3O_4 NCs.

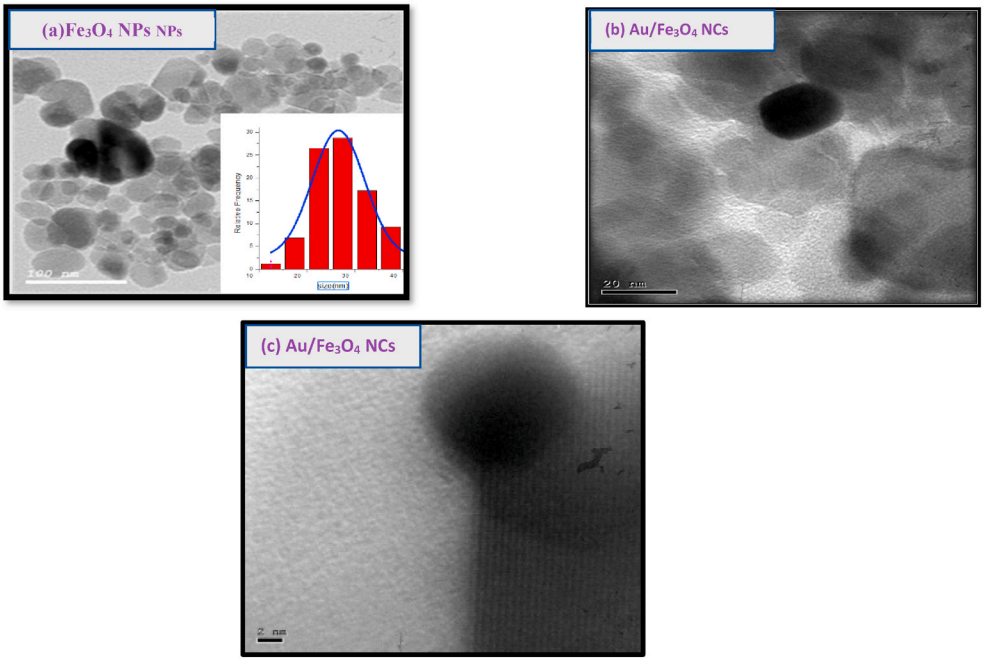

Fig. 6. (a)TEM images of Fe_3O_4 NPs, the inset is Particle size distribution histogram of Fe_3O_4 NPs, **(b)** TEM images of Au/Fe_3O_4 NCs and **(c)** TEM images of the synthesized Au/Fe_3O_4 NCs with high magnification.

nanoparticles. The average particle size of Fe_3O_4NPs was about 30 nm as shown the inset of Fig. 6 (a).

The structure and particle size of Au/Fe_3O_4 NCs were imaged by HRTEM, and are shown in Fig. 6(b). The addition of Au NPs, with a higher electron density than that of Fe_3O_4 NPs increases the metallic gold nanoparticles than that of Fe_3O_4 NPs, accordingly more electrons are transmitted in bright field showing symmetric dark spots with a spherical particle shape are observed. This is due to the decrease in the electronic spacing that is accompanied by an increase in the particle size. From the absorption spectra the particle size of Fe_3O_4 NPs can be estimated by the "Effective Mass Approximation" model (***EMA***) given by Ref. [40].

$$E_{gn} = E_{gb} + \frac{h^2}{8R^2}\left[\frac{1}{m_e} + \frac{1}{m_h}\right] - \frac{1.8e^2}{4\pi\varepsilon\varepsilon_0 R} \tag{7}$$

where, E_{gn} is the electronic band gap for Nano crystals, E_{gb} is the band gap of bulk Fe_3O_4 (0.1 eV), R is the average radius of nanoparticles. m_e is the electron effective mass ($100m_o$), m_h is the hole effective mass ($100m_o$), $m_o = 9.11*10^{-31}$ kg and ε is the dielectric constant for Fe_3O_4 sample [40]. The calculated particle size for Fe_3O_4 NPs presented in Table 1, is approximately the same as those obtained by TEM. The XRD pattern for Fe_3O_4 NPs and Au/Fe_3O_4 NCs (see Fig. 7) shows a strong

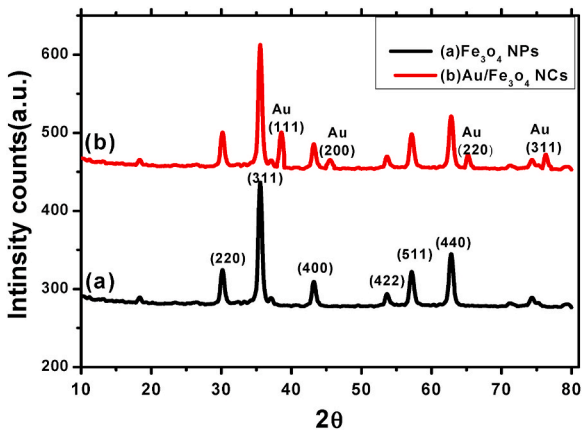

Fig. 7. *Shows the XRD spectra of synthesized* ***(a)*** Fe_3O_4 *NPs and* ***(b)*****Au/**Fe_3O_4 *NCs.*

diffraction peaks, that match well with the inverse cubic spinel reflection peak at $2\theta = 35.6$, and confirm the crystalline structure.

The average crystallite size was calculated using the Debye–Scherrer equation [41]**:**

$$D = \frac{0{\cdot}9\lambda}{B\cos\theta} \tag{8}$$

where **β** is the full-width at half-maximum (FWHM) value of XRD diffraction lines, the wavelength λ = 0.154056 nm and **θ** is the half diffraction angle of **2θ**. Fig. 7 presents the XRD patterns of Fe_3O_4 before and after the addition of Au NPs. All the peak positions of Au/Fe_3O_4 NCs remain unchanged compared with those of bare Fe_3O_4 NPs, with the addition, of some identified peaks that are corresponding to (111), (200), (220), and (311) planes [42]. The values of the average crystal size estimated from TEM, EMA and XRD are nearly the same as seen in Table 1. A suggested correlation between Crystallite size and optical energy gap can attributed to the spacing of the electronic level. As the crystallize size increases the spacing of the electronic level decreases and hence the band gap decreases as well. The addition of $AuNp_s$ To Fe_3O4NP_s as seen in Table 1,increased the Crystal size from 30 nm to 49 nm while the optical energy gap decreased from 1.73 eV to 1.68 EV which confirm the above mention suggestion.

3.4. *Effect of Au NPs on the desalination performance of* Fe_3O_4 *NPs*

Desalination is any process that removes excess salts and other minerals from water. The feed water for desalination process can be seawater. The thermal properties of Fe_3O_4 NPs and Au/Fe_3O_4 NCs were studied by the Photoacoustic (**PA**) technique of the liquid form samples in seawater. According to Poulet and Chambron for thermally thick samples, the PA amplitude ***(q)*** and frequency ***(f)***can be derived from the well-known equation [43]**:**

$$q = \frac{A\beta\mu_s}{2\pi fe\sqrt{(\beta\mu_s+1)^2+1}} \qquad \mu_s = \left(\frac{D}{\pi f}\right)^{\frac{1}{2}} \tag{9}$$

where ***(β)*** is the optical absorption coefficient, ***(e)*** is sample thermal effusivity, ***(μ)*** is thermal diffusion length and ***(A)*** is constant (not related to the sample). To compare the desalination performance of Fe_3O_4 NPs and Au/Fe_3O_4 NCs, the plot of the signal amplitude ***(q)*** versus ***(f)*** are displayed in Fig. 8. The fitting of Fig. 8 was used for determine the thermal diffusivity ***(D)*** and thermal effusivity ***(e)*** [44,45]. From these results it is possible to estimate the thermal conductivity ***(k)***, by using the following equation:

$$K = e\sqrt{D} \tag{10}$$

The results are given in Table 2.

As observed, the variation of the thermal conductivity ***(K)*** of Fe_3O_4 NPs increased with the addition of Au NPs in the Au/Fe_3O_4 NCs, this may be due to the localized surface plasmon resonance. This trend is supported by the data of the electrical conductivity seen in Fig. 5(b). Heat transfer occurs with a lower rate for materials of low thermal conductivity than in material of high thermal conductivity, this indicates that the driving force of Fe_3O_4 NPs significantly strengthened by the addition of Au NPs.In the present work, the water-based of Fe_3O_4 NPs and Au/Fe_3O_4 NCs were ultrasonically dispersed in seawater by using surfactant (Triton X-100) with concentration of 5mg/5 ml and 5 ml (NPs/water/surfactant respectively) [46]**.** The used surfactant is a low cost, non-toxite and it is masked by the high solution viscosity that prevent the particles from agglomerating. Therefor a quantitative difference in several properties including different in sedimentation rates with increasing surfactant can be observed. The photo-thermal conversion characteristics of a solar NPs were investigated under solar simulator, xenon lamp with (200Watt and irradiance (1000W/m^2) measured by power meter at different duration time of (60) minutes, as explained earlier in the experimental section and in Fig. 1(c).

The increase of the temperature of the nanofluid is higher than that of the base fluid (seawater) as shown in Fig. 9 which confirms that the strong absorption and the capturing of solar radiation, enhances the photo-thermal conversion efficiency, of Fe_3O_4 NPs and Au/Fe_3O_4 NCs

Table 2
The three thermal parameter of seawater, Fe_3O_4 NPs and Au/Fe_3O_4 NCs.

Sample	Thermal diffusivity (D) (Cm^2/s) × 10^{-7}	Thermal effectivity (e) ($Ws^{1/2}Cm^{-2}K^{-1}$)	Thermal conductivity (k) (W/Cm.K)
Seawater	**1.380**	**0.158**	**0.570**
Fe_3O_4 NPs	**1.624**	**0.186**	**0.671**
Au/Fe_3O_4 NCs	**1.863**	**0.213**	**0.785**

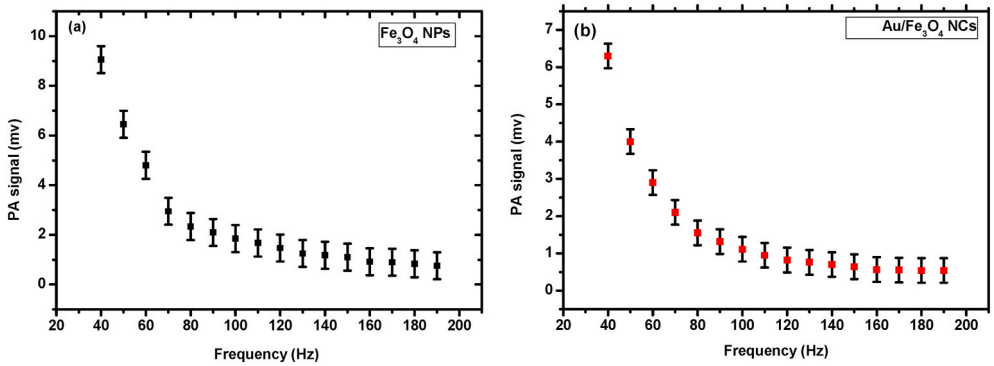

Fig. 8. Relation of (q) versus (f) for Fe_3O_4 NPs and Au/Fe_3O_4 NCs are respectively seen in (a)&(b).

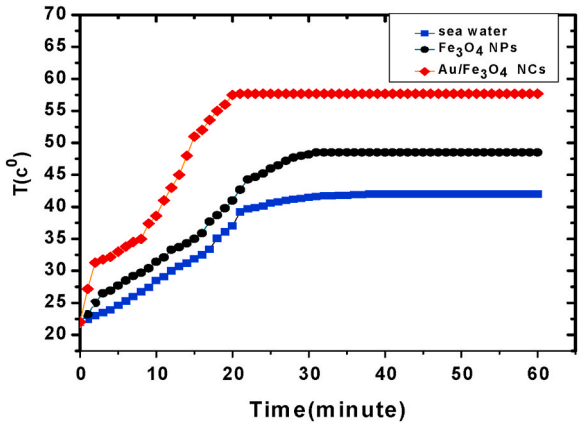

Fig. 9. The temperature distribution with time of Fe_3O_4 NPs, Au/Fe_3O_4 NCs and seawater.

compared to base fluid.

3.5. Thermal efficiency on desalination performance

The thermal efficiency is a dimensionless performance that helps in reducing the energy usage and costs for water desalination. Here, the solar radiation is uniform and the fluid depth is small so it can be assumed that the temperature of the NPs is the same as the surrounding fluid, measured by the thermocouple. The photo-thermal conversion efficiency ***(η)*** can be determined with the relation [47,48].

$$\eta = \frac{\Delta T c_w m_w}{\Delta t A G} \times 100\%$$

where, c_w and, m_w are the specific heat and the mass of the water, respectively, ΔT is the temperature difference of the nanofluid after an exposed time Δt; A is the irradiation area; G (W m^{-2}) is the irradiation intensity. The results of the photo-thermal conversion efficiency illustrated in Fig. 10 indicates the increase of the efficiency by adding the surfactant (Triton X-100) to Fe_3O_4 NPs and Au/Fe_3O_4 NCs.

Where the presence of nanoparticle suspended in seawater increases the absorption (direct absorption) of incident radiation more than that of pure seawater, upon adding Au NPs, hence efficiency of heating increases. This observation can also be related to oscillations of the delocalized conduction electrons, known as surface plasmons.

4. Conclusion

Fe_3O_4 NPs and Au/Fe_3O_4 NCs were successfully Synthesized and studied by simple co-precipitation method, in order to compare and explore the desalination performance. The micro structure and the crystal size were obtained and compared by using SEM, EDX, TEM, EMA and XRD. The absorption coefficient in the UV visible range (350–850 nm), was used for the determination of the optical energy gap, electronegativity, refractive index, optical and electrical conductivities. Moreover, the thermal diffusivity, thermal effusivity, thermal conductivity, and thermal efficiency have been conducted to investigate and compare the difference between the previously obtained results of Fe_3O_4 NP_S and Au/Fe_3O_4 NCs. The Nanofluids were prepared by dispersing Fe_3O_4 NPs and Au/Fe_3O_4 NCs in seawater by adding surfactant (Triton x-100) to improve the dispersion of nanofluid samples. According to the results the addition of Au NPs increased the thermal energy and the thermal efficiency. Further studies are needed for solving one of the major induced human problems affecting all the world.

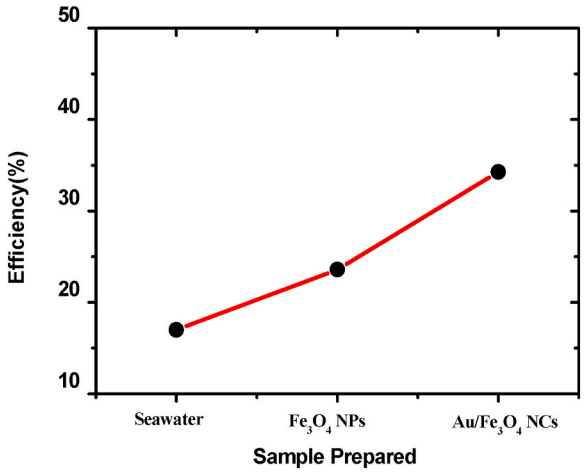

Fig. 10. Photo-thermal conversion efficiency of Fe_3O_4 NPs, Au/Fe_3O_4 NCs and seawater.

Authorship statement

The submission of the manuscript has been approved by all co author.

CRediT authorship contribution statement

M. Nabil: Measured and calculated the different parameters and revision. **Horia F.:** measured samples . **S.S. Fouad:** Writing – original draft. **Sohair Negm:** Revision.

Declaration of competing interest

The authors declare that they have no known competing financial interests or personal relationships that could have appeared to influence the work reported in this paper.

References

[1] Dahanayaka Madhavi, Bo Liu, Narasimalu Srikanth, Kun Zhou, Ionised graphene oxide membranes for seawater desalination, Desalination 496 (2020), 114637, https://doi.org/10.1016/j.desal.2020.114637.
[2] Faegh Meysam, Mohammad Behshad Shafii, Thermal performance assessment of an evaporative condenser-based combined heat pump and humidification-dehumidification desalination system, Desalination 496 (2020), 114733, https://doi.org/10.1016/j.desal.2020.114733.
[3] William Toh, YM Ang Elisa, Teng Yong Ng, Rongming Lin, Zishun Liu, An investigation on the effects of nanoplastic particles on nanoporous graphene membrane desalination, Desalination 496 (2020), 114765, https://doi.org/10.1016/j.desal.2020.114765.
[4] Yang Xu, Feng Duan, Yuping Li, Hongbin Cao, Junjun Chang, Haoliang Pang, Jianxin Chen, Enhanced desalination performance in asymmetric flow electrode capacitive deionization with nickel hexacyanoferrate and activated carbon electrodes, Desalination 514 (2021), 115172, https://doi.org/10.1016/j.desal.2021.115172.
[5] Ulbrich Karel, Hola Katerina, Subr Vladimir, Bakandritsos Airstides, Tucek Jiri and Zboril Radek "Targeted drug delivery with polymers and magnetic nanoparticles: covalent and noncovalent approaches, release control, and clinical studies, Chem. Rev. 116 (2016) 5338–5431, https://doi.org/10.1021/acs.chemrev.5b00589.
[6] Ashish Kumar Mishra, Ramaprabhu Sundara, Nano magnetite decorated multiwalled carbon nanotubes: a robust nanomaterial for enhanced carbon dioxide adsorption, Energy Environ. Sci. 4 (2011) 889–895, https://doi.org/10.1039/C0EE00076K.
[7] Jing Hu, Haiqiang Wang, Dongc Fan, Zhongbiao Wu, A new strategy for utilization of NIR from solar energy promotion effect generated from photo-thermal effect of Fe_3O_4@SiO_2 for photocatalytic oxidation of NO, Appl. Catal., B 204 (2017) 584–592, https://doi.org/10.1016/j.apcatb.2016.12.009.
[8] Alexander Govorov, Hugh Richardson, Generating heat with metal nanoparticles, Nano Today 2 (1) (2007|) 30–38, https://doi.org/10.1016/S1748-0132(07)70017-8.
[9] Amir Menbari, Alemrajabi, Amin Rezaei, Heat transfer analysis and the effect of CuO/Water nanofluid on direct absorption concentrating solar collector, Appl.

Therm. Eng. 104 (2016) 176–183, https://doi.org/10.1016/j.applthermaleng.2016.05.064.
[10] Todd Otanicar, Patrick E. Phelan, Ravi S. Prasher, Gary Rosengarten, Robert A. Taylor, Nanofluid-based direct absorption solar collector, J. Renew. Sustain. Energy 2 (3) (2010), 033102, https://doi.org/10.1063/1.3429737.
[11] Parvin Salma, Rehena Nasrin, M.A. Alim, Heat transfer and entropy generation through nanofluid filled direct absorption solar collector, Int. J. Heat Mass Tran. 71 (2014) 386–395, https://doi.org/10.1016/j.ijheatmasstransfer.2013.12.043.
[12] S. Vijayaraghavan, S. Ganapathisubbu, C. Santosh Kumar, Performance analysis of a spectrally selective concentrating direct absorption collector, Sol. Energy 97 (2013) 418–425, https://doi.org/10.1016/j.solener.2013.08.008.
[13] Y. Tian, C.Y. Zhao, A review of solar collectors and thermal energy storage in solar thermal applications, Appl. Energy 104 (2013) 538–553, https://doi.org/10.1016/j.apenergy.2012.11.051.
[14] Soteris Kalogirou, Solar thermal collectors and applications, Prog. Energy Combust. Sci. 30 (3) (2004) 231–295, https://doi.org/10.1016/j.pecs.2004.02.001.
[15] Sohair Negm, Talaat Hassan, Radiative and non-radiative decay of surface plasmons in thin metal films, Solid State Commun. 84 (1–2) (1992) 133–137, https://doi.org/10.1016/0038-1098(92)90310-6.
[16] Sanjay Vijayaraghavan, S. Ganapathisubbu, C. Santosh Kumar, Performance analysis of a spectrally selective concentrating direct absorption collector, Sol. Energy 97 (2013) 418–425, https://doi.org/10.1016/j.solener.2013.08.008.
[17] Todd Otanicar, Patrick E. Phelan, Ravi S. Prasher, Rosengarten Gary, Robert A. Taylor, Nanofluid-based direct absorption solar collector, J. Renew. Sustain. Energy 2 (3) (2010), 033102, https://doi.org/10.1063/1.3429737.
[18] Xuan Yimin, Huiling Duan, Qiang Li, Enhancement of solar energy absorption using a plasmonic nanofluid based on TiO_2/Ag composite nanoparticles, RSC Adv. 4 (31) (2014) 16206–16213, https://doi.org/10.1039/C4RA00630E.
[19] Saud Khashan, Sawsan Dagher, Salah addin Al Omari, Nacir Tit, Emad Elnajjar, Bobby Mathew, Ali Hilal-Alnaqbi, Photo-thermal characteristics of water-based Fe_3O_4@ SiO_2 nanofluid for solar-thermal applications, Mater. Res. Express 4 (5) (2017), 055701, https://doi.org/10.1088/2053-1591/aa6c15.
[20] Seid Reza Falsafi, Hadis Rostamabadi, Seid Mahdi Jafari, X-ray diffraction (XRD) of nano encapsulated food ingredients, in: Characterization of Nano Encapsulated Food Ingredients, Academic Press, 2020, pp. 271–293, https://doi.org/10.1016/B978-0-12-815667-4.00009-2.
[21] A. T El-Brolossy, S. Abdallah, T. Abdallah, Mona B. Mohamed, S. Negm, H. Talaat, Photoacoustic characterization of optical and thermal properties of CdSe quantum dots, Eur. Phys. J. Spec. Top. 153 (1) (2008) 365–368, https://doi.org/10.1140/epjst/e2008-00463-y.
[22] Badawi Ali, Najm Al-Hosiny, Said Abdallah, Sohair Negm, Talaat Hassan, Photoacoustic study of optical and thermal properties of CdTe quantum dots, J. Mater. Sci. Eng. 2 (2012) 1–6.
[23] T.A. El-Brolossy, S. Abdallah, T. Abdallah, H. Awad, M.B. Mohamed, S. Negm, H. Talaat, Photoacoustic spectroscopy characterization of CdSe quantum rods, Eur. Phys. J. Spec. Top. 153 (1) (2008) 369–372, https://doi.org/10.1140/epjst/e2008-00464-x.
[24] Yue Zhang, Zhi Yang, Di Yin, Yong Liu, ChunLong Fei, Rui Xiong, Jing Shi, GaoLin Yan, Composition and magnetic properties of cobalt ferrite nano-particles prepared by the co-precipitation method, J. Magn. Magn Mater. 322 (21) (2010) 3470–3475, https://doi.org/10.1016/j.jmmm.2010.06.047.
[25] Vinod Kumar, Anu Rana, M.S. Yadav, R.P. Pant, Size-induced effect on nano-crystalline $CoFe_2O_4$, J. Magn. Magn Mater. 320 (11) (2008) 1729–1734, https://doi.org/10.1016/j.jmmm.2008.01.021.
[26] Hsia Chih-Hao, Tai-Yen Chen, Dong Hee Son, Size-dependent ultrafast magnetization dynamics in iron oxide (Fe_3O_4) nanocrystals, Nano Lett. 8 (2) (2008) 571–576, https://doi.org/10.1021/nl072899p.
[27] Li Hongji, Li Yue, Dandan Wang, Junfu Wang, Jinyue Zhang, Wei Jiang, Tianyu Zhou, Chunbo Liu, Guangbo Che, Synthesis of hydrophilic SERS-imprinted membrane based on graft polymerization for selective detection of L-tyrosine, Sensor. Actuator. B Chem. 340 (2021), 129955, https://doi.org/10.1016/j.snb.2021.129955.
[28] Li Hongji, Junfu Wang, Haoqi Fang, Hongda Xu, Haochen Yu, Tianyu Zhou, Chunbo Liu, Guangbo Che, Dandan Wang, Hydrophilic modification of PVDF-based SERS imprinted membrane for the selective detection of L-tyrosine, J. Environ. Manag. 304 (2022), 114260, https://doi.org/10.1016/j.jenvman.2021.114260.
[29] Zhou Tianyu, Yanbo Wang, Tiantian Li, Hongji Li, Chunwei Yang, Dongshu Sun, Dandan Wang, Chunbo Liu, Guangbo Che, Fabricating magnetic hydrophilic molecularly imprinted resin with enhanced adsorption and recognition performance for targeted detecting chlorophenols in environmental water, Chem. Eng. J. 420 (2021), 129904, https://doi.org/10.1016/j.cej.2021.129904.
[30] Hanaa Zaka, S.S. Fouad, B. Parditka, A.E. bekheet, H.E. Atyia, Z. Erdélyi, Enhancements of dispersion optical parameters of Al2O3/ZnO thin flims fabricated by ALD, Sol. Energy 205 (2020) 79–87, https://doi.org/10.1016/j.solener.2020.05.025.
[31] M. Nabil, Shaimaa A. Mohamed, K. Easawi, Salah SA. Obayya, S. Negm, H. Talaat, M.K. El-Mansy, Surface modification of CdSe nanocrystals: application to polymer solar cell, Curr. Appl. Phys. 20 (3) (2020) 470–476, https://doi.org/10.1016/j.cap.2020.01.001.
[32] N.M. Ravindra, Preethi Ganapathy, Jinsoo Choi, Energy gap–refractive index relations in semiconductors–An overview, Infrared Phys. Technol. 50 (1) (2007), https://doi.org/10.1016/j.infrared.2006.04.001, 21 29.
[33] Stephen K. O' Leary, S.R. Johnson, P.K. Lim, The relationship between the distribution of electronic states and the optical absorption spectrum of an amorphous semiconductor: an empirical analysis, J. Appl. Phys. 82 (7) (1997) 3334–3340, https://doi.org/10.1063/1.365643.
[34] Indolia, R. S., and R. K. Verma. "Relationship between Refractive Index, Electronic Polarizability, Optical Energy Gap Optical Electronegativity and Plasmon Energy in I-Iii-Vi_2 and Ii-Iv-V_2 Groups of Semiconductors.".
[35] J.A. Duffy, Trends in energy gaps of binary compounds: an approach based upon electron transfer parameters from optical spectroscopy, J. Phys. C Solid State Phys. 13 (16) (1980) 2979, https://doi.org/10.1088/0022-3719/13/16/008.
[36] I.M. El Radaf, H.Y.S. Al-Zahrani, S.S. Fouad, M.S. El-Bana, Profound optical analysis for novel amorphous Cu_2FeSnS_4 thin films as an absorber layer for thin film solar cells, Ceram. Int. 46 (11) (2020) 18778–18784, https://doi.org/10.1016/j.ceramint.2020.04.195.
[37] S.S. Fouad, B. Parditka, M. Nabil, E. Baradács, S. Negm, H.E. Atyia, Z. Erdélyi, Bilayer number driven changes in polarizability and optical property in ZnO/TiO_2 nanocomposite films prepared by ALD, Optik 233 (2021), 166617, https://doi.org/10.1016/j.ijleo.2021.166617.
[38] S.S. Fouad, B. Parditka, A.E. Bekheet, H.E. Atyia, Z. Erdélyi, ALD of TiO_2/ZnO mutilayers towards the understanding of optical properties and polarizability, Opt Laser. Technol. 140 (2021), 107035, https://doi.org/10.1016/j.optlastec.2021.107035.
[39] El Radaf, H.Y.S. Al-Zahrani, S.S. Fouad, Profound optical analysis for novel amorphous Cu2FeSnS4 thin films as an absorber layer for thin film solar cells, Ceram. Int. 46 (11) (2020) 18778–18784.
[40] Lihua Bai, N.C. Giles, P.G. Schunemann, T.M. Pollak, K. Nagashio, R.S. Feigelson, Donor-acceptor pair emission near 0.55 eV in CdGeAs 2, J. Appl. Phys. 95 (9) (2004) 4840–4844, https://doi.org/10.1063/1.1687996.
[41] S. Benramache, O. Belahssen, A. Guettaf, A. Arif, Correlation between crystallite size–optical gap energy and precursor molarities of ZnO thin films, J. Semiconduct. 35 (4) (2014), 042001, https://doi.org/10.1088/1674-4926/35/4/042001.
[42] S.M. El-Bashir, O.A. Al Harbi, M.S. Al Salhi, Optimal design for extending the lifetime of thin film luminescent solar concentrators, Optik 125 (18) (2014) 5268–5272, https://doi.org/10.1016/j.ijleo.2014.06.046.
[43] P. Poulet, J. Chambron, R. Unterreiner, Quantitative photoacoustic spectroscopy applied to thermally thick samples, J. Appl. Phys. 51 (3) (1980) 1738–1742, https://doi.org/10.1063/1.327785.
[44] W. Aldama-Reyna, Jhenry F. Agreda-Delgado, M.A. Valverde-Alva, Luis M. Angelats-Silva, Photoacoustic study of changes in optical properties of colloids with silver nanoparticles produced by laser ablation, Int. J. Appl. Eng. Res. 13 (2) (2018) 1408–1414.
[45] F. Horia, Khaled Easawi, Reda Khalil, Said Abdallah, Mabrouk El-Mansy, Sohair Negm, Optical and Thermophysical characterization of Fe_3O_4 nanoparticle, in: IOP Conference Series: Materials Science and Engineering, vol. 956, IOP Publishing, 2020, 012016, https://doi.org/10.1088/1757-899X/956/1/012016, 1.
[46] Yang Yung-Jih, David S. Corti, Elias I. Franses, Effect of Triton X-100 on the stability of titania nanoparticles against agglomeration and sedimentation: a masked depletion interaction, Colloids Surf. A Physicochem. Eng. Asp. 516 (2017) 296–304, https://doi.org/10.1016/j.colsurfa.2016.12.026.
[47] Muhammad Wakil Shahzad, Muhammad Burhan, Doskhan Ybyraiymkul, Kim Choon Ng, Desalination processes' efficiency and future roadmap, Entropy 21 (1) (2019) 84, https://doi.org/10.3390/e21010084.
[48] Hui Zhang, Hui-Jiuan Chen, Xiaoze Du, Dongsheng Wen, Photothermal conversion characteristics of gold nanoparticle dispersions, Sol. Energy 100 (2014) 141–147, https://doi.org/10.1016/j.solener.2013.12.004.